Supreet S. Bahga[1]
Moran Bercovici[2]
Juan G. Santiago[1]

[1]Department of Mechanical Engineering, Stanford University, CA, USA
[2]Faculty of Mechanical Engineering, Technion-Israel Institute of Technology, Haifa, Israel

Received May 10, 2012
Revised June 30, 2012
Accepted July 9, 2012

Research Article

Robust and high-resolution simulations of nonlinear electrokinetic processes in variable cross-section channels

We present a model and an associated numerical scheme to simulate complex electrokinetic processes in channels with nonuniform cross-sectional area. We develop a quasi-1D model based on local cross-sectional area averaging of the equations describing unsteady, multispecies, electromigration-diffusion transport. Our approach uses techniques of lubrication theory to approximate electrokinetic flows in channels with arbitrary variations in cross-section; and we include chemical equilibrium calculations for weak electrolytes, Taylor–Aris type dispersion due of nonuniform bulk flow, and the effects of ionic strength on species mobility and on acid–base equilibrium constants. To solve the quasi-1D governing equations, we provide a dissipative finite volume scheme that adds numerical dissipation at selective locations to ensure both unconditional stability and high accuracy. We couple the numerical scheme with a novel adaptive grid refinement algorithm that further improves the accuracy of simulations by minimizing numerical dissipation. We benchmark our numerical scheme with existing numerical schemes by simulating nonlinear electrokinetic problems, including ITP and electromigration dispersion in CZE. Simulation results show that our approach yields fast, stable, and high-resolution solutions using an order of magnitude less grid points compared to the existing dissipative schemes. To highlight our model's capabilities, we demonstrate simulations that predict increase in detection sensitivity of ITP in converging cross-sectional area channels. We also show that our simulations of ITP in variable cross-sectional area channels have very good quantitative agreement with published experimental data.

Keywords:
Electrokinetics / High-resolution / Quasi-1D model / Simulation / Variable cross-section
DOI 10.1002/elps.201200264

1 Introduction

Electrokinetic techniques such as CZE and ITP are widely used for separation and preconcentration of chemical and biological species in a variety of fields including genetics, food analysis, and pharmacology [1, 2]. With ever increasing demand of improving sensitivity and resolution of electrokinetic techniques, computer simulations can play a pivotal role in exploring optimal experimental parameters. While there has been significant progress in numerical simulations of electrokinetic techniques, many electrokinetic problems are still computationally challenging. These may be optimization problems that may require a large number of solutions. These also include individual solutions of nonlinear electrokinetic processes, such as ITP, electromigration dispersion in CZE, and IEF, which can involve sharp gradients in ion concentrations. Challenges in simulating such nonlinear processes have further increased with need of simulating electrokinetic techniques in miniaturized lab-on-a-chip systems, which can involve high electric fields, sharp concentration gradients, and complex geometries compared to those of standard benchtop systems.

As in the case of other physical phenomena, accurate simulations of electrokinetic processes require: (i) correct modeling of underlying physics including species transport and chemical reactions, and (ii) accurate numerical schemes for solving the governing equations. Over the past three decades, significant improvements have been made in modeling of electrokinetic processes, beginning with work of Bier et al. [3]

Correspondence: Professor Juan G. Santiago, Department of Mechanical Engineering, Stanford University, 440 Escondido Mall, Building 530, Room 225, Stanford, CA 94305, USA
E-mail: juan.santiago@stanford.edu
Fax: +650 723-7657

Abbreviations: AMR-CESE, adaptive grid refinement-conservation element solution element; **LE**, leading electrolyte; **PLPE1**, phoenical low phase error-1; **SLIP**, symmetric limited positive; **TE**, trailing electrolyte

and Saville and Palusinski [4]. Bier et al. provided a unified approach for simulating a variety of electrokinetic techniques by formulating generalized electromigration-diffusion equations for weak electrolyte species. Later, in a related publication, Saville and Palusinski [4] extended the model of Bier et al. to ampholytes (with univalent ionization states only). Thereafter, several improvements to models of electrokinetic flows have been proposed, such as model of protein mobility by Mosher et al. [5], and model for ionic strength-dependent EOF by Thormann et al. [6]. More recently, Bercovici et al. [7] proposed a Taylor–Aris dispersion [8,9] type model to account for sample dispersion in presence of nonuniform EOF. Also, Hruska et al. [10] first proposed inclusion of ionic strength effects on species mobilities and ionic activity in electrophoresis simulations. They also added models of ionic strength effects in the SIMUL simulation tool. However, Hruska et al. did not report simulation results that accounted for ionic strength effects, and attributed this shortcoming to the high computational cost of such ionic strength corrections. Subsequently, Bahga et al. [11] described a faster implementation of ionic strength models similar to those described by Hruska et al., and presented detailed validation of their electrophoresis simulations (including ionic strength effects) using experimental data.

The second important issue associated with simulations of electrokinetic processes is the choice of numerical method, particularly the spatial discretization scheme. Several spatial discretization schemes have been proposed, and these can be roughly categorized as either nondissipative or dissipative schemes. Most common of all schemes is the second-order central difference scheme implemented on a uniform grid. This is a nondissipative approach and has been employed in well-known simulation tools such as SIMUL [10] and GENTRANS [12]. However, the second-order central difference scheme which these tools implement requires grid spacing which strictly meets the requirement of a grid Peclet number, $Pe_{\Delta x} = u\Delta x/D < 2$, to avoid unstable solutions [13]. For practical nonlinear 1D electrokinetic problems, this Peclet number requirement often translates to $\mathcal{O}(10^3)$ or more grid points. Simulations employing such large grids can take several hours to complete on current personal computers. To reduce the number of grid points and speed-up simulations, Bercovici et al. [14] presented a nondissipative, sixth-order compact finite difference scheme coupled with an adaptive grid refinement algorithm. The grid adaptation scheme of Bercovici et al. automatically clusters grid points in regions with large concentration gradients, optimizing computational time for high accuracy. The numerical scheme of Bercovici et al. allows for resolution of high wave numbers with lesser number of grid points, thereby ensuring both good resolution and stability with only $\mathcal{O}(10^2)$ grid points. Similar to all nondissipative schemes, the compact scheme (with or without adaptive grid refinement) does not guarantee monotonicity and may require judicious choice of grid size and adaptive grid parameters to ensure a nonoscillatory solution.

On the other hand, dissipative schemes result in more robust simulations by ensuring nonoscillatory solutions, but at the significant expense of higher numerical dissipation and lower accuracy (particularly in regions of high gradients). The most commonly used and easiest to implement dissipative scheme is the first-order upwind scheme [15]. Due to its lower accuracy, the upwind scheme when applied to electrokinetic problems with sharp gradients, such as ITP, results in low accuracy in the form of overly (artificially) diffused interfaces. This is true even with adaptive grid refinement [7]. Sounart and Baygents [16] improved the accuracy of dissipative schemes by using the flux corrected transport method [17], wherein numerical dissipation is added only to regions where solution needs to be stabilized. The numerical scheme of Sounart and Baygents, which they named phoenical low phase error-1 (PLPE1), results in second-order accuracy in regions with smooth solution and automatically switches to first-order accuracy in regions with local extrema in species concentrations, thereby insuring nonoscillatory solutions. However, the PLPE1 scheme is based on a uniform grid and the effects of numerical dissipation necessitate a number of grid points similar to that required by the second-order central scheme to obtain a converged solution. Recently Chou and Yang [18] proposed a space–time conservation element solution element scheme with adaptive mesh refinement (AMR-CESE) for simulations of nonlinear electrokinetic processes at high electric fields. The AMR-CESE scheme also adds limited numerical dissipation to ensure nonoscillatory behavior and provides more accurate solutions than the upwind scheme. However, the simulations of Chou and Yang showed that, even with their adaptive grid refinement, the AMR-CESE scheme was unable to capture sharp zone boundaries in ITP. Such comparisons of dissipative and nondissipative schemes show that existing numerical schemes for electrophoresis simulations can either ensure high resolution or guaranteed stability, but not both.

We also note that the majority of simulation studies of electrokinetic techniques, including all of those mentioned above, are based on 1D formulation of governing equations for species transport in uniform cross-section channels. Such simulations only predict streamwise variations in species concentrations and do not take into account spanwise variations in concentrations or channel cross section. The natural way of studying multidimensional effects in electrokinetic processes is through 2D or 3D simulations. For example, Choi et al. [19] used 2D simulations to demonstrate the effect of axially varying channel cross-sectional area on ITP focusing of proteins. Compared to 1D simulations, multidimensional simulations suffer from much longer computational time due to large number of grid points required to resolve spanwise variations in species concentrations. This limits the use of multidimensional simulations to ad hoc studies of specific geometries, and cripples their ability to serve as rapid, routine optimization, or design tools of electrokinetic assays. One approach of avoiding expensive 3D simulations for electrokinetic processes is to solve quasi-1D species transport equations based on area averaging of the corresponding 3D equations. Hruska et al. [20] employed a

quasi-1D approach in their SIMUL code and used it to simulate isoelectric trapping in compound channels made up of sections with different cross-sectional areas (each channel section having a uniform cross-sectional area). However, Hruska et al. did not provide details of their model or its numerical implementation. Later, Chou and Yang [21] presented an approximate analytical treatment describing electromigration and diffusion of species in variable cross-sectional area channels, and applied it to simulations of isoelectric focusing. However, the model of Chou and Yang incorrectly neglects diffusive current [7, 22], and does not account for advection and dispersion of species due to nonuniform bulk flow.

In the current work, we address directly these deficiencies in state-of-the-art simulations of electrokinetic processes. Our goal is to produce simulations which are both accurate and fast, and which apply to channels with variable cross-sectional area. The contributions of the current work are twofold: (i) a generalized model of quasi-1D electrokinetic processes in variable cross-sectional area channels, and (ii) a high-resolution and unconditionally stable finite volume scheme for solving the quasi-1D governing equations. We present a new quasi-1D formulation of governing equations which takes into account the effect of nonuniform cross-sectional area on species concentrations. Our generalized approach includes multispecies transport, chemical equilibrium calculations (for multivalent weak electrolyte species), nonuniform EOF, Taylor–Aris dispersion [8, 9], and the effect of ionic strength on species mobility and on acid–base equilibria. To solve the quasi-1D governing equations, we present a new approach based on a dissipative finite volume scheme which adds limited, localized numerical dissipation to guarantee nonoscillatory solutions. We also provide a novel grid refinement algorithm that improves the accuracy of our dissipative scheme by dynamically clustering grid points in regions with relatively high numerical dissipation. Coupled with adaptive grid refinement, our numerical scheme yields fast, stable, and high-resolution simulations using an order of magnitude less number of grid points compared to other dissipative schemes. As a demonstration, we present detailed simulations using our numerical method for various nonlinear electrokinetic problems including electromigration dispersion in CZE and ITP. For the more challenging ITP simulations, we consider both uniform and axially varying cross-section channels. For all simulations involving uniform cross-section channels, we compare our results with the experimentally validated sixth-order compact scheme of Bercovici et al. [7, 11, 14]. For simulations of ITP focusing in variable cross-section channels, we provide detailed comparison and validation with experiments of Bahga et al. [23]. We have integrated the quasi-1D formulation of species transport equations and the current numerical scheme in our existing electrokinetics solver SPRESSO [7]. The physical mechanisms addressed by the latest version of the code are summarized in Fig. 1. The source code (and an executable version) can be downloaded for free from http://microfluidics.stanford.edu/spresso.

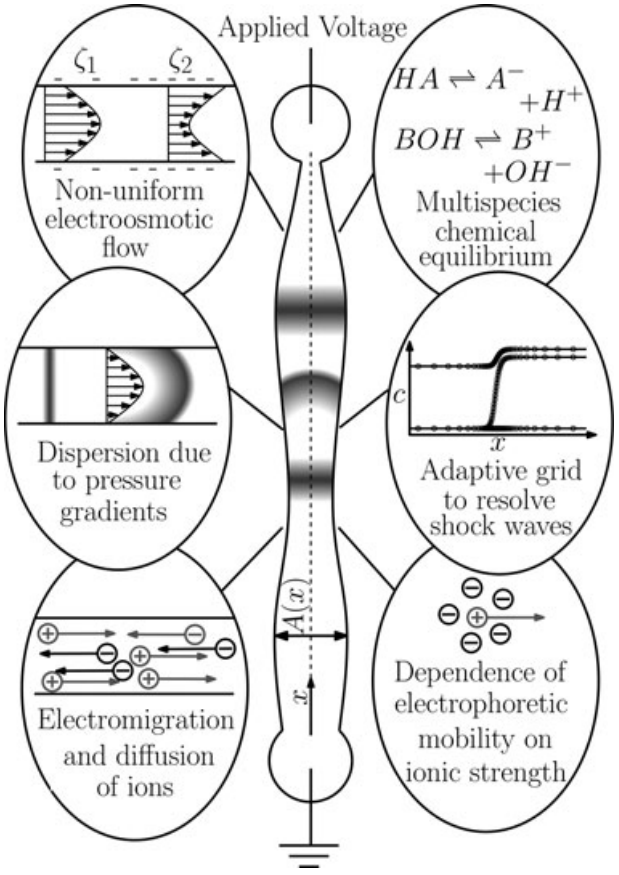

Figure 1. Schematic summarizing various physical features of the current simulation code. Our simulation code solves area-averaged electromigration-diffusion equations for nonlinear electrophoresis problems and can handle slow axial variations in channel cross-section. The code uses a finite volume scheme with limited numerical dissipation, coupled with an adaptive grid refinement scheme to ensure accurate and nonoscillatory solutions. We have integrated the quasi-1D formulation of species transport equations and the numerical scheme presented here into our open-source electrophoresis solver SPRESSO [7, 11, 14]. Other numerical schemes available in SPRESSO include a sixth-order compact scheme [7, 14], a second-order central difference scheme, and a first-order upwind scheme. The code also includes physical modules for calculation of multispecies chemical equilibrium, correction of electrophoretic mobilities and acid–base equilibria for finite ionic strength, and estimation of effective dispersion coefficients using a model for Taylor–Aris type dispersion [8, 9].

2 Materials and methods

2.1 Mathematical model

2.1.1 Quasi-1D model for electrokinetics

Here we present a quasi-1D model for electrokinetic transport of ionic species in channels with axially varying cross-sectional area. We begin with 3D advection-diffusion equations for concentration of each ionic state z within each

species family i,

$$\frac{\partial c_{i,z}}{\partial t} + \nabla \cdot (\mathbf{u}c_{i,z} + \mu_{i,z}c_{i,z}\mathbf{E}) = \nabla \cdot (D_{i,z}\nabla c_{i,z}) + R_{i,z},$$
$$i = 1, \ldots, N, \quad z = n_i, \ldots, p_i. \tag{1}$$

Here $c_{i,z}$ denotes the concentration, $\mu_{i,z}$ the electrophoretic mobility, $D_{i,z}$ the molecular diffusivity, and $R_{i,z}$ the rate of production (or consumption) of the corresponding species. The valence state, z, of species family i ranges between n_i and p_i, which are, respectively, the minimum and maximum valence states corresponding to that species family. Here "species family" refers to all ionization states of a species, so that, for example, i = arginine has four ionization states, $z = -1$, 0, $+1$, and $+2$ and hence $n_i = -1$ and $p_i = +2$. In Eq. (1) vector fields $\mathbf{u} = u_x\hat{\mathbf{x}} + u_y\hat{\mathbf{y}} + u_z\hat{\mathbf{z}}$ and $\mathbf{E} = E_x\hat{\mathbf{x}} + E_y\hat{\mathbf{y}} + E_z\hat{\mathbf{z}}$ denote the velocity of bulk fluid and the electric field, respectively. Since the net production rate of species i is zero, summing Eq. (1) over all its valence states and assuming each $D_{i,z}$ is spatially uniform (but distinct for different species and their valence states), yields a conservative set of equations in terms of the total (analytical) concentration of species, $c_i = \sum_z c_{i,z}$,

$$\frac{\partial c_i}{\partial t} + \nabla \cdot (\mathbf{u}c_i + \mu_i c_i \mathbf{E}) = \nabla^2 (D_i c_i), \quad i = 1, \ldots, N. \tag{2}$$

Here μ_i and D_i denote the effective mobility and diffusivity of species family i, respectively, and are defined relative to its ionization states as:

$$\mu_i = \sum_{z=n_i}^{p_i} g_{i,z}\mu_{i,z}, \quad D_i = \sum_{z=n_i}^{p_i} g_{i,z}D_{i,z}, \quad g_{i,z} = \frac{c_{i,z}}{c_i}, \tag{3}$$

where $g_{i,z}$ denotes fraction of species i, ionized in valence state z. That is, the effective mobility and diffusivity of a particular species is the weighted mean of mobilities and molecular diffusivities of all its ionization states with weights $g_{i,z}$. As noted by Saville and Palusinksi [4], in typical electrophoresis experiments migration and diffusion of species occur at much longer time scales compared to the time scale of acid–base dissociation reactions. Therefore, knowing the total concentrations, c_i, the concentration of various ionization states, $c_{i,z}$, can be obtained by assuming local chemical equilibrium between different chemical species [7, 14]. Later in Section 2.1.2, we discuss the chemical equilibrium calculations in more detail.

To obtain quasi-1D transport equations from the governing equations in three dimensions, we integrate Eq. (2) over the channel cross section. Noting that the flux of species into the channel walls is zero, the area-averaged equations can be represented as:

$$\frac{\partial}{\partial t}(A(x)\,\bar{c}_i) + \frac{\partial}{\partial x}\left(A(x)\,\overline{u_x c_i} + A(x)\,\overline{\mu_i c_i E_x}\right)$$
$$= \frac{\partial}{\partial x}\left(A(x)\,\overline{\frac{\partial}{\partial x}(D_i c_i)}\right), \quad i = 1, \ldots, N, \tag{4}$$

where $A(x)$ denotes the cross-sectional area and the overbar symbol denotes area-averaged quantities. We note Eq. (4) exactly describes the species transport in terms of the area-averaged quantities. However, to bring closure to these equations we use the following assumptions: (i) we assume that the fluid velocity and the electric field are locally axial (neglecting multidimensional effects in the slowly varying cross section), (ii) we capture the order of magnitude of streamwise diffusive fluxes using the axial gradient of area-averaged species concentrations, $\bar{c}_i$, with diffusivity, D_i. These assumptions are typical of lubrication theory [24] and hold well when the characteristic length scale in transverse direction, h, is much smaller than the characteristic length scale in streamwise direction, ℓ, that is, $h/\ell << 1$. In the present case, h is the characteristic height (or diameter) of the channel and ℓ is the axial length scale over which gradient in species concentration persists. With the aforementioned assumptions, Eq. (4) can be simplified to:

$$\frac{\partial}{\partial t}(A(x)\,\bar{c}_i) + \frac{\partial}{\partial x}\left(A(x)\,\bar{u}_x\bar{c}_i + A(x)\,\mu_i\bar{c}_i\,\overline{E_x}\right)$$
$$= \frac{\partial}{\partial x}\left(A(x)\,\frac{\partial}{\partial x}(D_i\bar{c}_i)\right), \quad i = 1, \ldots, N. \tag{5}$$

In the Supporting Information, we show by rigorous asymptotic analysis that, in absence of bulk flow, for relatively narrow channel cross sections ($\varepsilon = h/\ell << 1$), dispersion due to nonaxial electric field in axially varying cross section is only $\mathcal{O}(\varepsilon^2)$. That is, in absence of nonuniform bulk flow, Eq. (5) gives only $\mathcal{O}(\varepsilon^2)$ error in the description of species transport. Whereas in presence of both nonuniform bulk flow and electric field, Eq. (5) captures only an order of magnitude approximation of diffusive fluxes. In the Supporting Information, we also show that Taylor–Aris dispersion [8, 9] due to nonuniformity in bulk flow can also be taken into account approximately by replacing D_i with a Taylor–Aris dispersion coefficient based on the local nonuniform bulk flow velocity. Besides dispersive effects of nonuniform bulk flow, the current model also accounts for dispersion due to axially nonuniform electric field in variable cross-sectional area channels (see Supporting Information). We note that our analysis and simulations do neglect secondary effects of temperature gradients and electrohydrodynamic flows that may arise and couple with electrokinetic processes associated with nonuniform cross-sectional area channels.

While the governing equations, Eq. (5), correctly model species transport in variable cross-section channels when species concentrations vary over length scales longer than the characteristic channel thickness, they can also be used in situations where diffusion is limited to sharp concentration gradients. This situation is typical of ITP where analyte zones with locally uniform concentrations are separated by sharp zone boundaries. For such cases, Eq. (5) can be used to accurately predict the concentrations, lengths, and migration velocities of various ITP zones, and approximately capture the features of diffusive zone boundaries in variable cross-section channels. We note that for uniform cross-section channels with no bulk flow, Eq. (5) exactly describes the species transport, regardless of the length scales over which concentration gradients persist.

The governing equations, given by Eq. (5), form a coupled set of N parabolic partial differential equations for total concentrations of species. The coupling between transport equations for different species comes from the local streamwise electric field, $\overline{E_x}$, which depends on the concentrations of all species via local electrical conductivity. The governing equation for electric field, $\overline{E_x}$, can be derived by invoking current conservation and assuming electroneutrality in the bulk fluid. The latter condition implies that we also neglect advection currents in current conservation. Accounting for only electromigration and diffusion currents in current conservation, the governing equation for electric field is given by

$$\frac{\partial}{\partial x}\left(A(x)\,\bar{\sigma}\,\overline{E_x} - A(x)\,\frac{\partial S}{\partial x}\right) = 0, \tag{6}$$

where $\bar{\sigma}$ denotes the area-averaged conductivity and $\partial S/\partial x$denotes the diffusive current density. Expressions of $\bar{\sigma}$ and S are given by

$$\bar{\sigma} = \sum_{i=1}^{N}\sum_{z=n_i}^{p_i} z\bar{c}_{i,z}\mu_{i,z}F, \qquad S = \sum_{i=1}^{N}\sum_{z=n_i}^{p_i} z\bar{c}_{i,z}D_{i,z}F, \tag{7}$$

where F is the Faraday's constant. By integrating Eq. (6), streamwise electric field, $\overline{E_x}$, can be expressed in terms of applied current, $I(t)$, as:

$$\overline{E_x} = \frac{1}{\bar{\sigma}}\left(\frac{I(t)}{A(x)} + \frac{\partial S}{\partial x}\right). \tag{8}$$

Note that the above relation for $\overline{E_x}$ holds irrespective of the means of applying external electric field (by current or voltage sourcing). For current sourcing, current $I(t)$in Eq. (8) is known a priori. Whereas, for problems where a known potential is applied across the channel (ΔV), $I(t)$ is obtained by simply integrating Eq. (8) over the physical domain, x, and using the fact that $\int \overline{E_x}\mathrm{d}x = -\Delta V$. Note that, even though we assume bulk electroneutrality to derive Eq. (6), the electric field can vary in the streamwise direction. See Hickman [25] for further discussion of the assumption of bulk electroneutrality. Briefly, electroneutrality in these systems holds in considering species conservation over regions with length scales significantly greater than the Debye screening length [26].

2.1.2 Chemical equilibrium and ionic strength effects

Analytes and BGE in electrokinetic experiments are very often weak electrolytes. To model electromigration and diffusion of weak electrolyte species, it is necessary to calculate the local pH of the electrolyte mixture using acid–base equilibrium theory. This is because effective mobility (μ_i) and effective diffusivity (D_i) of a species family (as defined in Eq. (3) are strong functions of the ionization fractions, $g_{i,z}$, which themselves depend on the pH of solution. As noted by Saville and Palusinski [4], time scales at which species migrate and diffuse are much longer than the time scale at which chemical equilibrium is established. Therefore, concentrations of each of various ionic states can be obtained by solving algebraic chemical equilibrium equations, and these can be used to calculate effective mobilities and diffusivities using Eq. (3).

Chemical equilibrium calculations for electrolyte solutions containing arbitrary number of ampholytes have been discussed in detail by Bercovici et al. [7, 14]. Here, we briefly outline the necessary algebraic equations for calculating the pH and the ionization fractions. Following Bercovici et al. [7, 14], the fraction of species i in valence state z, $g_{i,z}$, can be described in terms of hydronium ion concentration, c_H, and equilibrium constants, $K_{i,z}$, as:

$$g_{i,z} = \frac{c_{i,z}}{c_i} = \frac{L_{i,z}c_H^z}{\sum_{z_i=n_i}^{p_i} L_{i,z}c_H^z}, \quad L_{i,z} = \begin{cases} \prod_{z'=z}^{-1} K_{i,z'} & z<0, \\ 1 & z=0, \\ \prod_{z'=0}^{z-1} K_{i,z'}^{-1} & z>0 \end{cases} \tag{9}$$

The remaining equation required to obtain hydronium ion concentration, c_H, comes from the assumption of electroneutrality of the bulk solution:

$$\sum_{i=1}^{N}\sum_{z=n_i}^{p_i} zc_{i,z} + c_H - \frac{K_w}{c_H} = 0, \tag{10}$$

where K_w denotes the equilibrium constant for dissociation of water. Given the total concentrations of all species, $c_i, \quad i = 1, \ldots, N$, Eqs. (9) and (10) can be solved iteratively to obtain the pH (or c_H), and the ionization fractions, $g_{i,z}$. These calculations are performed at every time step of simulation to update the values of effective mobility and diffusivity of species using Eq. (3).

In general, effective mobility also depends on the ionic strength of electrolyte solution, albeit weakly compared to its dependence on pH. Ion mobility decreases below its ideal value at infinite dilution as ionic strength increases, and this effect is more pronounced for multivalent species compared to univalent ions [11]. As shown by Bahga et al. [11], changes in ionic strength can affect the relative magnitude of species mobility and cause changes of zone order in electrophoresis experiments. To take into account the effect of ionic strength on effective mobility of species, we correct the mobilities and the ionic activity for finite ionic strength using the extended Onsager–Fuoss model [27] and the extended Debye–Huckel theory [28], respectively. In the current work, we use the existing implementation of aforementioned chemical equilibrium and ionic strength correction models in the SPRESSO simulation tool [11]. Details of numerical implementation, verification, and experimental validation of chemical equilibrium and ionic strength correction models in SPRESSO are presented elsewhere [7, 11, 14]. The SPRESSO source code and documentation are available for free at http://microfluidics.stanford.edu/spresso.

2.2 Numerical method

We discretize the governing equations, given by Eq. (5), using a finite volume method based on the symmetric limited positive (SLIP) scheme of Jameson [29]. The SLIP scheme presented here is second-order accurate in regions with smooth solution and automatically switches to first-order accuracy in regions with a local extrema or oscillations. This is achieved by first constructing a stable, globally first-order scheme and then adding limited "anti-diffusion" terms in regions with smooth solution to recover second-order accuracy. Thus, numerical dissipation associated with first-order accuracy stabilizes the solution in the regions where it tends to become oscillatory and anti-diffusion improves the accuracy of numerical scheme to second order in regions where the solution is smooth. The spatial discretization in the SLIP scheme insures unconditional stability while maintaining relatively higher order (second order) accuracy at the majority of locations. This is in contrast to the nondissipative schemes such as the second-order central scheme employed by Hruska et al. [10] and the sixth-order compact scheme of Bercovici et al. [14], which do not guarantee nonoscillatory solutions on coarse grids. Another advantage of the current scheme over previous finite difference-based schemes for simulations of electrokinetic processes is that, being a finite volume scheme, our approach explicitly conserves the mass of analytes irrespective of the grid density. The latter feature is especially useful in systems with varying cross-sectional area channels.

Many nonlinear electrokinetic processes such as ITP and electromigration dispersion in CZE involve sharp gradients in species concentrations. For such nonlinear electrokinetics problems, the current scheme adds numerical dissipation to regions with high gradients, resulting in artificially diffused interfaces. Therefore, to improve the accuracy of our scheme while using less grid points, we employ an adaptive grid algorithm that recruits grid points from regions with lower numerical dissipation (usually regions with smooth solution) and clusters them in regions with high numerical dissipation. Our finite volume scheme in conjunction with adaptive grid refinement yields high accuracy solutions with lower number of grid points while mathematically guaranteeing nonoscillatory solution. In Section 2.2.1, we present a conservative formulation of governing equations on a uniform computational grid using a nonlinear mapping between the physical and the computational domain. In Section 2.2.2, we present the spatial discretization scheme for the transformed governing equations in computational domain. In Section 2.2.3, we also discuss the grid adaptation procedure which determines the mapping between physical and computational space. In Section 2.2.4, we present a brief discussion of time integration scheme and the treatment of boundary conditions.

2.2.1 Governing equations in computational space

As is typical of simulations with dynamically adapting mesh, we transform the governing equations, Eqs. (5) and (6), from an adapting physical grid to a uniform, stationary computational grid. After computing the solution on the computational grid, we map the solution back on to the dynamically adapting physical grid. We define a smooth nonlinear mapping function, $x = H(\xi, t)$, that relates locations in physical space, x, to the corresponding locations in computational space, ξ, at any particular time, t. The Jacobian and the mesh velocity corresponding to this mapping are given by

$$J = \frac{\partial x}{\partial \xi} = \frac{\partial H}{\partial \xi}, \quad V = \frac{\partial x}{\partial t} = \frac{\partial H}{\partial t}. \tag{11}$$

We then express the partial derivatives occurring in the governing equations, Eq. (5), using the chain rule. For example:

$$\begin{aligned} \left.\frac{\partial g}{\partial t}\right|_x &= \left.\frac{\partial g}{\partial t}\right|_\xi - \frac{\partial g}{\partial \xi}\frac{\partial \xi}{\partial x}\frac{\partial x}{\partial t} = \left.\frac{\partial g}{\partial t}\right|_\xi - \frac{V}{J}\frac{\partial g}{\partial \xi}, \\ \frac{\partial g}{\partial x} &= \frac{\partial g}{\partial \xi}\frac{\partial \xi}{\partial x} = \frac{1}{J}\frac{\partial g}{\partial \xi}, \end{aligned} \tag{12}$$

where g is a generic scalar field. Applying the transformations defined in Eq. (12) to Eq. (5), we obtain quasi-1D advection-diffusion equations in the computational domain:

$$\begin{aligned} J\frac{\partial}{\partial t}(A\bar{c}_i) - V\frac{\partial}{\partial \xi}(A\bar{c}_i) + \frac{\partial}{\partial \xi}\left(A\bar{u}_x\bar{c}_i + A\mu_i\bar{c}_i\overline{E_x}\right) \\ = \frac{\partial}{\partial \xi}\left(\frac{A}{J}\frac{\partial}{\partial \xi}(D_i\bar{c}_i)\right), \quad i = 1, \ldots, N. \end{aligned} \tag{13}$$

In many cases the cross-sectional area, A, is not defined analytically and is known only at the grid points in physical space at the beginning of simulation. Therefore, as grid points adapt in physical space over time, it is necessary to evaluate cross-sectional area at newly adapted grid points. Noting that the channel walls are rigid and the cross-sectional area in physical domain is invariant with time, we solve

$$J\frac{\partial A}{\partial t} - V\frac{\partial A}{\partial \xi} = 0 \tag{14}$$

to evaluate cross-sectional area at new locations in physical space. In the physical domain, x, Eq. (14) simply translates to $\partial A/\partial t = 0$.

In order to construct a conservative numerical scheme, we reformulate Eqs. (13) and (14) in a conservative form using the identity, $\partial J/\partial t = \partial V/\partial \xi (= \partial^2 x/\partial t \partial \xi$, evident from Eq. (11)). The conservative form of governing equations in computational domain is given by

$$\begin{aligned} &\frac{\partial}{\partial t}(J\,A\bar{c}_i) + \frac{\partial f_i}{\partial \xi} = 0, \quad i = 1, \ldots, N \\ &f_i = A\left(-V\bar{c}_i + \bar{u}_x\bar{c}_i + \mu_i\bar{c}_i\overline{E_x} - \frac{1}{J}\frac{\partial}{\partial \xi}(D_i\bar{c}_i)\right), \end{aligned} \tag{15}$$

$$\frac{\partial}{\partial t}(J\,A) - \frac{\partial}{\partial \xi}(V\,A) = 0. \tag{16}$$

Similarly, we transform the governing equation for electric field, Eq. (6), from physical to computational domain to obtain:

$$\frac{\partial}{\partial \xi}\left(A\bar{\sigma}\overline{E_x} - \frac{A}{J}\frac{\partial S}{\partial \xi}\right) = 0. \tag{17}$$

Eqs. (15)–(17) can now be discretized on a uniform stationary computational grid using any finite volume scheme. However, to close the system, it remains to determine the mapping between physical and computational domain, $x = H(\xi, t)$. In the current work we use an adaptive grid refinement scheme that minimizes numerical dissipation added by the spatial discretization scheme to stabilize the solution. Therefore, we first discuss the spatial discretization scheme in Section 2.2.2 and subsequently derive the necessary time evolution equation for the mapping function, $H(\xi, t)$, in Section 2.2.3.

2.2.2 Spatial discretization

We use the SLIP scheme of Jameson [29] for spatial discretization of the transformed governing equations, Eqs. (15) and (16). Construction of SLIP scheme involves addition of limited anti-diffusive terms to a low-order (first order in the current work) scheme in a way that the anti-diffusive terms cancel out low-order numerical diffusion in regions with smooth solution. The resulting scheme yields second-order accuracy in regions with smooth solution and reverts to first-order accuracy in regions with local extrema or oscillations. Limited anti-diffusion is affected by a flux limiter, which acts as a switch to turn off the anti-diffusive terms when solution shows a local extremum or spurious oscillations. As shown by Jameson [29] the SLIP scheme mathematically guarantees monotonicity and so ensures nonoscillatory solutions.

We discretize the computational domain of length L into n number of cells with thickness $\Delta\xi = L/(n-1)$ and cell centers at $\xi_j = j\Delta\xi$, $j = 1, \ldots, N$. The governing equations for species concentration, Eq. (15), spatially discretized using the SLIP scheme are given by

$$\Delta\xi\frac{\partial}{\partial t}\left(\left(J\,A\bar{c}_i\right)_j\right) + F_{i,j+1/2} - F_{i,j-1/2} = 0,$$
$$j = 2, \ldots, N-1, \tag{18}$$

where $F_{i,j+1/2}$ is the numerical flux of species i across the $(j+1/2)$-th cell edge that separates cells j and $(j+1)$. The numerical flux $F_{i,j+1/2}$ is defined as:

$$F_{i,j+1/2} = \frac{1}{2}\left(f_{i,j} + f_{i,j+1}\right) - d_{i,j+1/2}, \tag{19}$$

where $f_{i,j}$ denotes the flux of species i (defined in Eq. (15) evaluated at cell center, j,and $d_{i,j+1/2}$ is the numerical dissipation flux added to stabilize the solution. The numerical dissipation flux, $d_{i,j+1/2}$, is defined as a combination of diffusive and anti-diffusive fluxes:

$$d_{i,j+1/2} = \alpha_{j+1/2}\left(\Delta\bar{c}_{i,j+1/2} - L\left(\Delta\bar{c}_{i,j+3/2}, \Delta\bar{c}_{i,j-1/2}\right)\right),$$

$$\Delta\bar{c}_{i,j+1/2} = \bar{c}_{i,j+1} - \bar{c}_{i,j}, \tag{20}$$

where $L\left(\Delta\bar{c}_{i,j+3/2}, \Delta\bar{c}_{i,j-1/2}\right)$ is the limited average of $\Delta\bar{c}_{i,3+1/2}$ and $\Delta\bar{c}_{i,j-1/2}$. Later, we discuss how limited average regulates the amount of anti-diffusion added to the solution based on the local smoothness of solution. In Eq. (20), $\alpha_{j+1/2}$ is a scalar parameter that regulates the amount of numerical dissipation. Jameson [29] showed that the SLIP scheme guarantees nonoscillatory solutions when $\alpha_{j+1/2} > 0.5\max_i\left|\lambda_{i,j+1/2}\right|$, where λ denotes the characteristic waves speeds of the system of governing equations. In the Supporting Information, we discuss the choice of $\alpha_{j+1/2}$ in detail for electrokinetic systems. There we show that choosing $\alpha_{j+1/2} \geq 0.5\max_i\left|A\bar{u}_x + \mu_i I/\bar{\sigma} - VA\right|_{j+1/2}$ is sufficient to ensure nonoscillatory solutions for nonlinear electrokinetics problems.

Similar to the spatial discretization of species transport equation, Eq. (15), the equation for evaluating cross-sectional area at newly adapted grid points, Eq. (16), can be discretized using the SLIP scheme as:

$$\Delta\xi\frac{\partial}{\partial t}\left(\left(JA\right)_j\right) + F_{A,j+1/2} - F_{A,j-1/2} = 0. \tag{21}$$

Here $F_{A,j+1/2}$ is the numerical flux at $(j+1/2)$-th cell edge and is given by

$$F_{A,j+1/2} = -\frac{1}{2}\left(\left(VA\right)_{j+1} + \left(VA\right)_j\right)$$
$$-\beta_{j+1/2}\left(\Delta A_{j+1/2} - L\left(\Delta A_{j+3/2}, \Delta A_{j-1/2}\right)\right). \tag{22}$$

In Eq. (22), $\Delta A_{j+1/2} = A_{j+1} - A_j$, and $\beta_{j+1/2}$ is a factor analogous to $\alpha_{j+1/2}$ and chosen such that $\beta_{j+1/2} > 0.5\left|V_{j+1/2}\right|$ to avoid spurious oscillations.

It remains to define an appropriate limited average, L, in Eqs. (20) and (22) which acts as a switch between first- and second-order accurate schemes. Following Jameson [29], in the current work we use a family of limited averages (or flux limiter), defined by

$$L\left(v, w\right) = \frac{1}{2}\left(v + w\right)\left(1 - \left|\frac{v - w}{|v| + |w|}\right|^q\right), \tag{23}$$

where q is a positive integer. For $q = 1$ and 2, $L\left(v, w\right)$ reduces to the well-known minmod and Van Leer limiters [30], respectively. Further, as q increases the limited average defined in Eq. (23) approaches the arithmetic mean of v and w. Note that $L\left(v, w\right) = 0$ if v and w have opposite signs; else $L(v, w) > 0$. All simulations shown here used a limited average defined by Eq. (23) and with $q = 4$. The effect of limited anti-diffusion, $L(\Delta\bar{c}_{i,j+3/2}, \Delta\bar{c}_{i,j-1/2})$, on the numerical dissipation flux, $d_{i,j+1/2}$, in Eq. (20) can be interpreted as follows: In the regions where concentration profiles, $\bar{c}_i$, are smooth and have no local extrema $\Delta\bar{c}_{i,j+3/2}$ and $\Delta\bar{c}_{i,j-1/2}$ have same signs. In such a case, a limited anti-diffusion $L\left(\Delta\bar{c}_{i,j+3/2}, \Delta\bar{c}_{i,j-1/2}\right) > 0$ is applied and this cancels out the leading term of $\Delta\bar{c}_{i,j+1/2}$ in Eq. (20) to provide $\mathcal{O}\left(\Delta\xi^3\right)$ numerical dissipation flux. This translates to $\mathcal{O}\left(\Delta\xi^2\right)$ discretization error in regions with smooth solution. On the contrary, if

concentration, $\bar{c}_i$, attains a local extremum at j-th grid point, then $\Delta\bar{c}_{i,j+3/2}$ and $\Delta\bar{c}_{i,j-1/2}$ have opposite signs, which sets the anti-diffusive term $L\left(\Delta\bar{c}_{i,j+3/2}, \Delta\bar{c}_{i,j-1/2}\right) = 0$. The absence of anti-diffusion in regions with local extrema results in $\mathcal{O}\left(\Delta\xi^2\right)$ numerical dissipation in Eq. (18) and correspondingly first-order accuracy of spatial discretization. Therefore, the current numerical scheme selectively adds higher numerical dissipation in regions with steep gradients and local extrema compared to regions with relatively smooth concentration profiles. This localized switching of accuracy insures stable solutions without adding excessive numerical dissipation to regions with smooth features. However, relatively lower accuracy of the current scheme at local extrema and sharp gradients in species concentrations can result in artificially diffused concentration peaks and interfaces. To circumvent this issue, in Section 2.2.3, we present an adaptive grid refinement scheme which improves the overall accuracy of our scheme by migrating grid points from regions with lower to higher numerical dissipation.

2.2.3 Adaptive grid refinement

Adaptive grid refinement can be framed as a calculus of variations problem of minimizing a known cost functional. We follow the approach of Bercovici et al. [14] and define our cost functional as:

$$K(x) = \int_0^L w(\xi)\, J\, \mathrm{d}x = \int_0^L w(\xi)\, J^2 \mathrm{d}\xi, \tag{24}$$

where J is the Jacobian defined in Eq. (11) and $w(\xi)$ is a weighting function that regulates grid density at different locations in the physical domain. When the cost functional, K, is minimized, the grid density increases (and correspondingly J decreases) in regions where the weighting function acquires large values. As shown by Jameson [31], the cost functional in Eq. (24) is minimized when the gradient $G = 0$, where G is defined as:

$$G \equiv 2\frac{\partial}{\partial\xi}\left(w(\xi)\, J\right) = 2\frac{\partial}{\partial\xi}\left(w(\xi)\,\frac{\partial x}{\partial\xi}\right). \tag{25}$$

Solving $G = 0$ requires solution of a boundary value problem for $x(\xi, t)$ at every time step, followed by interpolation of solution to the newly adapted grid points in physical space. To avoid this computationally expensive approach of computing an absolute minimum of the cost functional at every time step, we suffice with time-marching in the direction of minimum by solving

$$\frac{\partial x}{\partial t} = -\kappa G. \tag{26}$$

Here κ is a positive scalar parameter that controls the migration speed of grid points in physical space. In practice the gradient, G, is smoothed before solving Eq. (26). See Bercovici et al. [14] and Jameson [31] for more details on smoothing the gradient and choosing appropriate value of κ.

Typically, the weighting function, $w(\xi)$, in Eq. (24) is chosen as the local magnitude of concentration gradient so as to adapt the grid points in regions with large concentration gradients. For example, Bercovici et al. [14] used a weighting function based on concentration gradient to stabilize their nondissipative compact scheme, which otherwise becomes unstable near sharp gradients for coarse grids. In contrast, the current scheme guarantees unconditional stability, but does so by adding lower order numerical dissipation. Therefore, to improve the accuracy of our numerical scheme, we propose a new weighting function which forces the grid points to cluster in regions where the numerical scheme adds higher numerical dissipation to stabilize the solution. The current grid refinement scheme therefore not only clusters grid points at locations with steep gradients, but also does so at extrema of concentration peaks where our numerical scheme is first-order accurate. Note that adaptive grid scheme of Bercovici et al., in contrast, will not preferentially cluster grid points at peak extrema, where the gradient is zero but numerical dissipation is high. Furthermore, for problems with variable cross-sectional area, we augment the weighting function based on numerical dissipation to simultaneously aggregate grid points in regions with more rapid cross-sectional area variation. We define the weighting function at grid point j, $w_j(\xi)$, as

$$\begin{aligned} w_j(\xi) &= \gamma_1 \frac{\max_i \left|\tilde{d}_{i,j+1/2} - \tilde{d}_{i,j-1/2}\right|}{\max_{i,j}\left|\tilde{d}_{i,j+1/2} - \tilde{d}_{i,j-1/2}\right|} + \gamma_2 \frac{\partial A/\partial\xi|_j}{\max_j \left.\partial A/\partial\xi\right|_j} + \frac{J_j}{\max_j J_j}, \\ \tilde{d}_{i,j} &= \Delta\bar{c}_{i,j+1/2} - L\left(\Delta\bar{c}_{i,j+3/2}, \quad \Delta\bar{c}_{i,j-1/2}\right). \end{aligned} \tag{27}$$

Here $\tilde{d}_{i,j}$ is proportional to the numerical dissipation added to discretized transport equation for species i at grid point j. Here, the first two terms on the right hand side of Eq. (27) tend to cluster grid points in regions with higher numerical dissipation and variation in cross-sectional area, respectively. Whereas, the third term in the definition of $w_j(\xi)$ in Eq. (27) scales inversely with grid density and avoids excessive depletion of grid points from a particular region; it also prevents the weighting function from being zero in case of a constant solution in a uniform cross-section channel. The factors γ_1 and γ_2 in Eq. (27) are scalar constants that can be tuned to assign relative importance to the aforementioned criteria for clustering grid points. For example, when $\gamma_1 >> \gamma_2$ grid points will preferentially adapt in regions with higher numerical dissipation compared to the regions with nonuniform cross-sectional area. In the Supporting Information, we use scaling analysis to derive simple guidelines for choosing factors γ_1 and γ_2. For general electrophoresis problems, we recommend values of order $\mathcal{O}\left(10^2 - 10^3\right)$ each for γ_1 and γ_2.

2.2.4 Boundary conditions and time integration

In electrokinetics simulations where species concentration profiles evolve far from the domain boundaries, it is often sufficient to use fixed concentration values (Dirichlet boundary conditions) at the boundaries. This approach has been used in the great majority of previous studies on electrophoresis simulations, including those by Palusinski et al. [32] and Dose and Guiochon [13]. However, simulations with fixed boundary conditions require a large computational domain so as to avoid interaction of propagating concentration waves with domain boundaries. Significant computational efficiency can be obtained by employing characteristic boundary conditions, which allow concentration waves to leave the domain without reflection from domain boundaries. Such boundary conditions allow use of smaller computational domain for simulating only the regions of interest. For example, in many ITP simulations it is computationally efficient to solve the governing equations in a frame of reference moving with analyte zones. In the current work, we use characteristic boundary conditions for electrokinetics simulations as described by Bercovici et al. [14]. We refer interested readers to Section 3.4 of Bercovici et al. for details on formulation and implementation of these boundary conditions.

Nonlinear electrokinetic processes can exhibit complex phenomenon involving changes in characteristic speed of concentration waves over time. For simulations of such processes, it is difficult to obtain a priori estimates of time steps to ensure stable time integration. Furthermore, choosing a fixed conservative time step for simulating an electrokinetics problem with multiple temporal scales can lead to wastage of computational time. Therefore, we use an adaptive time stepping scheme to integrate spatially discretized governing equations, Eqs. (18) and (21), along with the equation governing adaptive grid refinement, Eq. (26). In the current work, we employ the third-order Runge–Kutta–Bogacki–Shampine (RK23) time-stepping scheme which uses an embedded second-order scheme to estimate the local truncation error and adapt the time step.

3 Results and discussion

We implemented the numerical algorithms discussed in Section 2.2 in Matlab and integrated them with our existing open-source electrokinetics solver, SPRESSO [7]. We used the existing, experimentally validated modules for chemical equilibrium and ionic strength effects for calculation of pH, effective mobilities, and diffusivities. The results presented here were obtained using Matlab release version 2007b running on 32 bit Windows XP operating system. An AMD 2.3 GHz Athlon 64 X2 4400+ with 2 GB RAM was used as the computing platform.

In this section, we first present simulations of CZE and ITP in uniform cross-section channels. We compare our simulation results with the upwind and sixth-order compact schemes; both previously implemented in SPRESSO. We then present simulations of ITP focusing and separation of analytes in converging cross-section channels and show the effect of nonuniform cross-sectional area on species concentration and analyte zone lengths. We also present validation of our ITP simulations in variable cross-section channels with detailed experimental data of Bahga et al. [23]. For simulations other than those shown for validation against experimental data (in Fig. 6), we neglected the effect of ionic strength on the mobility and ionic activity of species.

3.1 Electromigration-dispersion in capillary zone electrophoresis

We first present simulations of a benchmark problem involving electromigration dispersion in CZE using the SLIP scheme and compare the computed concentration profiles with results from the upwind and sixth-order compact schemes. This benchmark problem was originally proposed by Ermakov et al. [33] and subsequently adopted by Sounart and Baygents [16] and Bercovici et al. [7] to test the ability of their numerical schemes. This test case involves CZE separation of two high concentration analytes in a uniform cross-section channel. As high concentration analytes migrate along the channel, they perturb the local conductivity of the electrolyte solution which is otherwise governed by uniform BGE in CZE. The nonuniformity in local electric field associated with variation in conductivity causes sharpening of analyte zone edge on one side and broadening on the other. Therefore, this model simulation serves as an example to demonstrate the ability of our numerical scheme to provide stable and high-resolution solutions in presence of sharp gradients. For simulations using the SLIP scheme, we used adaptive grid refinement based on minimizing numerical dissipation (see Section 2.2.3). On the other hand, for simulations using the upwind and compact sixth-order schemes, we used the existing implementation in SPRESSO with grid refinement procedure based on clustering grid points in regions with large concentration gradients.

We performed simulations using the SLIP, upwind and sixth-order compact schemes in a 200 mm long channel discretized with 400 grid points. The BGE was 12 mM tris ($pK_a = 8.076$ and $\mu = 29.5 \times 10^{-9}$ m^2 V^{-1} s^{-1}) and 20 mM acetic acid ($pK_a = 4.75$ and $\mu = -42.4 \times 10^{-9}$ m^2 V^{-1} s^{-1}). The weak base analytes aniline ($pK_a = 4.8$ and $\mu = 32.5 \times 10^{-9}$ m^2 V^{-1} s^{-1}) and pyridine ($pK_a = 5.16$ and $\mu = 30 \times 10^{-9}$ m^2 V^{-1} s^{-1}) were initially introduced in the channel at a distance of 30 mm from the left boundary, in form of Gaussian-shaped zones with 1 mM peak concentration. For each numerical scheme, we performed two sets of simulations corresponding to current densities of 2547 and 10 190 A m^{-2}. We chose mesh adaptation parameters so as to ensure similar grid density for the SLIP and compact schemes. Minimum grid spacing used for simulations with current density of 2547 and 10 190 A m^{-2} was $\Delta x \approx 30$ μmand $\Delta x \approx 15$ μm, respectively.

Figure 2A and B shows concentration profiles of fully separated analyte peaks at current density of 2547 and 10 190 A m^{-2}, respectively, computed using the upwind, the SLIP (with parameter $q = 4$), and the sixth-order compact scheme. At lower current density, all three schemes yield nonoscillatory solution. Figure 2A shows that both SLIP and compact schemes accurately resolve the analyte peaks, including the sharp leading interfaces of analyte zones. In contrast, the upwind scheme yields overly diffused analyte peaks because of its lower (first order) accuracy throughout the domain. Figure 2B shows that at higher current density of 10 190 A m^{-2}, the upwind and the SLIP scheme still produce nonoscillatory solution as they both ensure monotonicity. Again, the upwind scheme results in artificially diffused peaks due to high numerical dissipation associated with its first-order accuracy. On the other hand, for the simulation conditions used here, the sixth-order compact scheme of Bercovici et al. [14] yields spurious oscillations due to unresolved wave numbers. Unlike the compact scheme, the SLIP scheme yields stable solution at current density of 10 190 A m^{-2} with similar grid density. The SLIP scheme dampens unresolved wave numbers to ensure nonoscillatory solution. This dampening of unresolved wave numbers indeed affects the solution accuracy, but the resulting solution is still a better representation of the exact solution (with small error) compared to the nonphysical oscillatory solution obtained from the higher-order compact scheme.

Figure 2A and B also shows preferential distribution of grid points at sharp interfaces due to adaptive grid refinement. We note that dynamically adapting grid employed here has significant advantages over fixed uniform grid as the former helps reduce the number of grid points to obtain a converged solution. As an illustration, for the case shown in Fig. 2A, simulation using the PLPE1 scheme of Sounart and Baygents [16] required a uniform grid with 2000 grid points ($\Delta x = 100$ μm) for convergence. In comparison, for the same case we used only 400 grid points and yet obtained three times higher resolution ($\Delta x = 30$ μm). In other words, simulations using a numerical scheme with uniform grid would require 16 times more grid points in order to equal the spatial resolution of our current simulations.

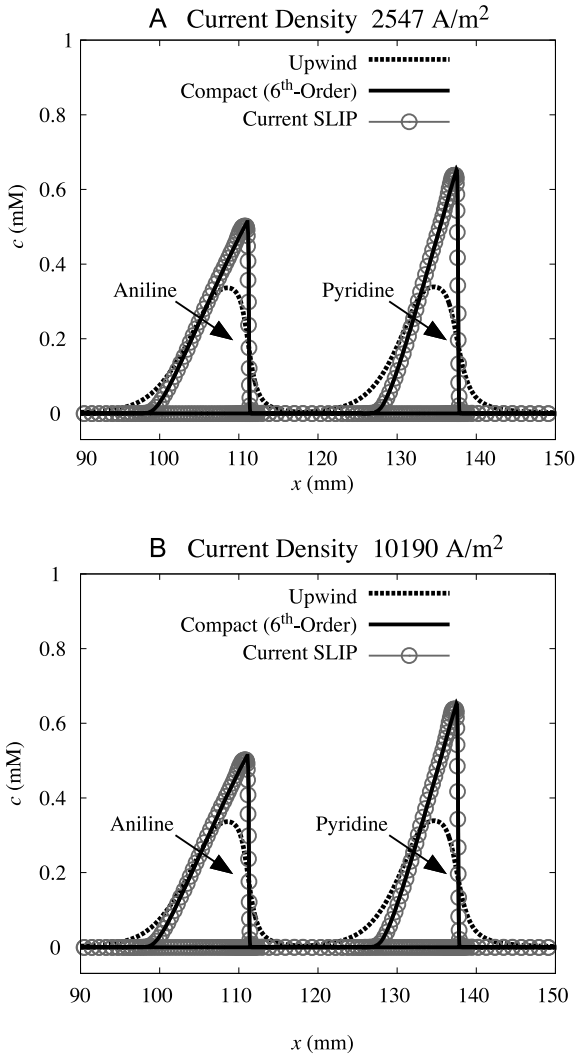

Figure 2. Simulations of electromigration dispersion in CZE using the upwind, sixth-order compact, and current SLIP spatial differencing schemes. Plots (A) and (B) show simulations of CZE separation of aniline and pyridine at current densities of 2547 and 10 190 A m^{-2}, respectively. For both cases, the upwind and the current SLIP scheme yield nonoscillatory solutions as they both ensure monotonicity. (A) At relatively lower current density of 2547 A m^{-2} the sixth-order compact scheme of Bercovici et al. [14] is stable and accurately resolves the sharp leading interfaces of analyte peaks. On the other hand, the upwind scheme is overly diffusive due to its first-order accuracy throughout the domain. Concentration profiles computed using the SLIP scheme (for $q = 4$) compare well with the results using the more accurate sixth-order compact scheme. (B) At higher current density of 10 190 A m^{-2}, the SLIP scheme still yields nonoscillatory and physically consistent solution. In comparison, for similar grid density, the compact scheme yields nonphysical oscillations. For these simulations we used 200 mm long computational domain with 400 grid points. We chose mesh adaptation parameters so as to ensure similar grid density for the SLIP and compact schemes. The minimum grid spacing used for simulations shown in (A) and (B) are $\Delta x \approx 30$ μm and $\Delta x \approx 15$ μm, respectively.

3.2 Resolving sharp gradients in ITP

Next, we demonstrate the ability of our numerical scheme to accurately resolve sharp zone boundaries in ITP. In ITP, analytes focus and can separate between zones of high effective mobility leading electrolyte (LE) ions and low effective mobility trailing electrolyte (TE) ions. When present in sufficient amount, analytes in ITP focus into distinct, purified zones with locally uniform zone concentrations. This mode is termed as "plateau mode ITP" [34] and is characterized by sharp zone boundaries separating adjacent analyte zones with locally uniform concentrations. However, when analytes are present in small amounts, their zone concentrations do not reach the plateau values. Instead, the analytes focus into

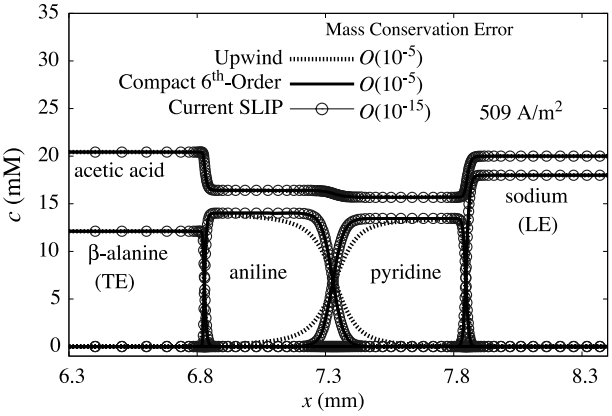

Figure 3. Simulation results of focusing and separation of aniline and pyridine in plateau mode ITP. The plot shows comparison of concentration profiles computed using the upwind, sixth-order compact, and the current SLIP differencing schemes. Simulations using the upwind and compact finite differencing used adaptive grid refinement based on clustering grid points in regions with large concentration gradients, as described by Bercovici et al. [14]. Whereas simulations with the current SLIP scheme used adaptive grid refinement procedure to minimize numerical dissipation as described in Section 2.2.3. Concentration profiles computed using the current SLIP scheme compare well with those obtained using more accurate sixth-order compact scheme. In particular, plateau concentrations and zone boundary thickness obtained using the current scheme agree well with the results from compact scheme. In comparison, the upwind scheme is more dissipative and so yields a nonconverged solution due to artificial broadening of zone boundaries. Plot also shows how the grid refinement procedure adapts the grid points (shown in circles) from regions of uniform concentrations to sharp zone boundaries. Our finite volume scheme is based on conservative formulation of governing equations and conserves mass of focused analytes with $\mathcal{O}(10^{-15})$ accuracy. The simulations used 15 mm long domain with 300 grid points. We solved the equations in a frame of reference moving with ITP zones so as to reduce the number of grid points.

peaks with widths determined by the boundary thickness of neighboring zones. The latter mode is termed "peak mode ITP" [34].

To test our numerical scheme for simulating ITP problems, we consider the benchmark case of plateau mode ITP, originally proposed by Ermakov [33]. This test case involves cationic ITP focusing of two weak base analytes (aniline and pyridine). This test case is particularly interesting as it has been used previously to compare the performance of several numerical schemes, including those by Martens et al. [15], Sounart and Baygents [16], Yu et al. [35], Bercovici et al. [7], and Chou and Yang [18].

We performed two sets of simulations, each using the SLIP, the upwind and the compact scheme, at current densities of 509 and 2260 A m^{-2}. For these simulations the LE was 18 mM sodium hydroxide ($pK_a = 13.7$, $\mu = 51.9 \times 10^{-9}$m^2 V^{-1} s^{-1}) and 20 mM acetic acid, and the TE was 40 mM β-alanine ($pK_a = 3.3$, $\mu = 36 \times 10^{-9}$m^2 V^{-1} s^{-1}) and 20 mM acetic acid. Figure 3 shows comparison of concentration profiles computed using the upwind, the SLIP, and the sixth-order compact scheme at current density of 509 A m^{-2}. For this set of simulations, we used a frame of reference moving with ITP zone to minimize the number of grid points. The computational domain was 15 mm long and we used 300 grid points for spatial discretization. Simulations using the upwind and the compact scheme used adaptive grid refinement scheme of Bercovici et al. [14] wherein grid points cluster in regions with large concentration gradients. For the current SLIP scheme, we used an adaptive grid refinement procedure to minimize numerical dissipation (see Section 2.2.3). As shown in Fig. 3, concentration profiles computed using the SLIP scheme compare well with those obtained using the more accurate and previously verified sixth-order compact scheme. The current scheme is able to predict correctly the plateau concentrations and the thickness of diffusive zone boundaries. In comparison, the upwind scheme is only first-order accurate throughout the domain and yields a nonconverged solution marred with artificial broadening of zone boundaries.

The distribution of grid points in Fig. 3 illustrates how our adaptive grid algorithm preferentially clusters grid points at sharp interfaces. At these sharp interfaces, the SLIP scheme adds higher numerical diffusion to suppress spurious oscillations. The reduction in numerical dissipation due to adaptive grid refinement enables our dissipative SLIP scheme to predict thickness of sharp zone boundaries with a resolution comparable with the nondissipative compact scheme. We note that besides the advantage of unconditional stability, the current scheme conserves mass significantly more precisely than the finite difference schemes (both compact and upwind) discussed by Bercovici et al. [7, 14]. This is because our numerical scheme is based on a finite volume method for conservative formulation of governing equations, and hence conserves mass irrespective of the grid size. For example, for simulations shown in Fig. 3, the current scheme conserves mass with $\mathcal{O}\left(10^{-15}\right)$ accuracy, while the upwind and the compact scheme (previously implemented in SPRESSO) conserve mass with relatively lower accuracy of $\mathcal{O}\left(10^{-5}\right)$.

In Fig. 4, we show the zone boundary thickness predicted by our numerical scheme at current density of 2260 A m^{-2} versus the number of grid points, and compare it with simulation results of Sounart and Baygents [16], Yu et al. [35], Bercovici et al. [7], and Chou and Yang [18]. We used the same simulation conditions as those in the aforementioned numerical studies. Briefly, the analytes (aniline and pyridine) were injected as 1 mm plugs at a concentration of 10 mM in a 40 mm long capillary, and subsequently allowed to migrate for 42 s. As a fair comparison, we performed each of these simulations in a stationary frame of reference and varied the number of grid points from 200 to 4000. As shown in Fig. 4, the compact scheme of Bercovici et al. provides a converged solution with grid independent zone boundary thickness when more than 400 grid points are used. Below 400 grid points, the compact scheme shows nonphysical oscillations due to unresolved wave numbers [7]. Due to its nondissipative nature and high accuracy, we here use predictions from the sixth-order compact scheme as baseline for comparison of other

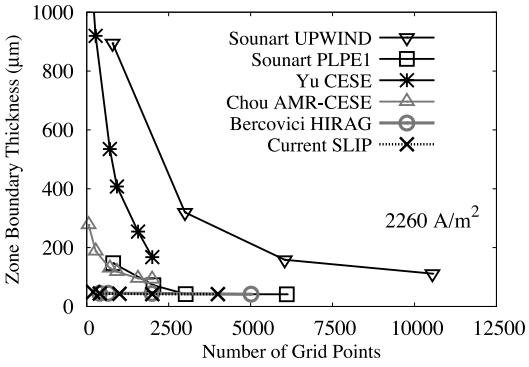

Figure 4. Comparison of six numerical schemes in predicting zone boundary thickness between aniline and pyridine zones in ITP. Here zone boundary thickness is defined as the length over which species concentration changes from 1% to 99% of its plateau value. Electrolyte chemistry and simulation parameters are the same as that for simulation shown in Fig. 3, except for a higher current density of 2260 A m^{-2} in this case. The upwind scheme is highly dissipative and does not show convergence of boundary thickness even when $\mathcal{O}(10^4)$ grid points are used. The conservation element solution element (CESE) scheme of Yu et al. [35] and the PLPE1 scheme of Sounart and Baygents [16] are less dissipative than the upwind scheme. The CESE scheme with adaptive grid refinement (AMR-CESE scheme of Chou and Yang [18]) shows improved accuracy compared to the CESE scheme and follows a convergence trend similar to the PLPE1 scheme. The high resolution adaptive grid (HIRAG) scheme of Bercovici et al. [7, 14] is nondissipative and coupled with adaptive grid shows convergence for all grids on which it produces a nonoscillatory solution. Note that the HIRAG scheme does not ensure monotonicity and results in oscillatory solutions for $\lesssim$400 grid points. The current SLIP scheme, which preserves monotonicity and minimizes numerical dissipation using adaptive grid refinement, provides essentially grid independent prediction of interface thickness. Compared with other schemes, the SLIP scheme provides relatively accurate nonoscillatory solution with only 200 grid points. The data for the upwind and PLPE1 schemes was digitized from Sounart and Baygents et al. [16], and data for CESE and AMR-CESE schemes was digitized from Chou and Yang [18].

numerical schemes. Figure 4 shows that zone boundary thickness computed using dissipative schemes of Sounart and Baygents [16], Yu et al. [35], and Chou and Yang [18] shows strong dependence on grid size. For a higher number of grid points, the numerical dissipation in dissipative schemes decreases and improves the prediction of zone boundary thickness.

In comparison, the current numerical scheme is able to predict the interface thickness with reasonable accuracy. Compared to equivalent uniform grid schemes, such as PLPE1 of Sounart and Baygents [16] which takes ~2500 grid points to converge, the current scheme converges to the solution of the higher accuracy compact scheme in 400 grid points. The improved grid convergence behavior of our scheme compared to other dissipative schemes is due to the adaptive grid refinement procedure, which minimizes numerical dissipation. We note that, unlike the compact scheme of Bercovici et al. [7] which results in spurious oscillations below 400 grid points, our scheme yields stable solution with even 200 grid points. This stability with just 200 grid points is possible due to the numerical dissipation; however, it comes at a cost of ~15% error in computed interface thickness. Users of this scheme should, of course, verify grid convergence of predicted solutions for simulations that require high accuracy.

3.3 Effect of variable channel cross section on plateau mode ITP

In Section 3.2, we benchmarked our numerical scheme with the previously verified and experimentally validated sixth-order compact scheme of Bercovici et al. [7, 11, 14] for ITP problems in uniform cross-section channel. We now examine the effect of axially varying cross-sectional area on analyte focusing in ITP. Using variable cross-sectional area channels is a common and effective way of increasing sample loading and hence detection sensitivity in ITP [23, 36]. In this technique, analytes are first allowed to focus in a large cross-section region and subsequently analytes are detected after they migrate into a narrow cross-section region. The large volume of the large cross-sectional area region increases the amount of analytes focused prior to their detection. Later, when the analyte zones transition from the large to small cross-section region, their zone lengths increase to conserve mass, providing higher detection sensitivity.

While ITP in variable cross-section channels has been used in several experimental studies for high-sensitivity detection of ionic species, there has been limited work on simulations of this process. The majority of electrophoresis solvers, including SIMUL [10], GENTRANS [12], and older versions of SPRESSO [7], are based on 1D formulation of advection-diffusion equations applicable in uniform cross-sectional area channels. Bahga et al. [23] presented a 1D model for ITP in variable cross-sectional area channels based on the assumption of negligible diffusion. However, the diffusion-free model of Bahga et al. is well suited for predicting analyte zone concentrations and zone lengths only when analyte zones are significantly longer than diffusive zone boundaries. To the best of our knowledge, simulations of ITP in variable cross-section geometry including both advective and diffusive fluxes have been limited to computationally expensive multidimensional numerical studies [19]. Here we present first-of-their-kind quasi-1D simulations which account for advection and diffusion of species in ITP along with variation in channel cross section.

We first examine the problem of plateau mode ITP focusing of two analytes in a channel with axially varying cross-section. The channel geometry, shown in Fig. 5, consists of fivefold reduction in cross-sectional area. The electrolyte chemistry was the same as that in ITP simulations shown in Figs. 3 and 4. Simulation results presented in Fig. 5 show analyte zones at three locations as they migrate along the channel. Analytes first focus in the large cross-section region in the form of thin plateau zones. As the analyte zones transition from large to small cross-section region, their zone lengths increase inversely with

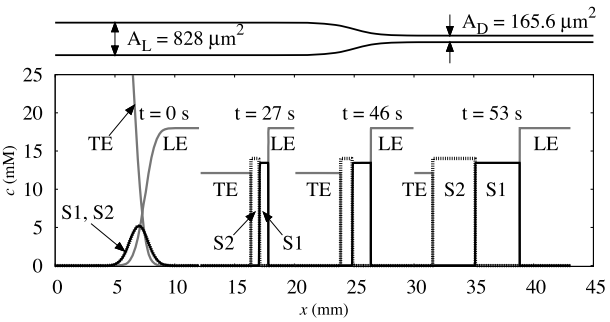

Figure 5. Simulation showing focusing and separation of pyridine and aniline in plateau mode ITP as it approaches and travels through a converging channel with fivefold cross-sectional area reduction. Initially, at $t = 0$, pyridine (S1) and aniline (S2) are injected as overlapping, diffuse Gaussian peaks between the leading electrolyte (LE) and trailing electrolyte (TE) zones. Upon application of an electric field, analytes (S1 and S2) focus between LE and TE zones ($t = 27$ s). Due to high initial amount of analytes and relatively high current densities, both S1 and S2 quickly form plateau-like zones in the large cross-section region. As the analyte zones transition from the large to small cross-section region ($t = 46$ s), their zone lengths increase inversely with decrease in cross-sectional area. Note that the plateau concentration of analytes does not depend on channel cross section as this is simply set by the area-independent Jovin–Alberty regulating functions [37, 38]. Later at $t = 53$ s, when analyte zones fully migrate into the narrow cross-section region, their zone lengths reach new steady values. Analyte zones elongate five times due to a fivefold reduction in cross-sectional area. Electrolyte chemistry is the same as that for simulations in Fig. 3. Simulations used a 60 mm long computational domain with 450 grid points and a constant applied current of 1 μA.

decreasing cross-sectional area. After the analyte zones completely transition to the small cross-section region, their zone lengths attain steady values, which are about five times larger than the corresponding zone lengths in the large cross-sectional area region. However, variation in cross-sectional area does not affect the plateau concentration of analyte zones. This is because the maximum concentration of each analyte zone (the plateau concentration) is set by the regulating function established by the LE mixture (here, the appropriate regulating functions are the Jovin and Alberty functions [37, 38]) which does not depend on the channel cross-section. We note that non-uniform electric fields resulting from variation in channel cross-sectional area can lead to temporary dispersion of ITP zone boundaries. Our quasi-1D model correctly accounts for dispersive effect of nonuniform electric field in variable crosssectional area channels, and we provide simulations results in the Supporting Information to demonstrate this.

Next, we verify and validate our quasi-1D simulations of ITP in converging cross-section channels, respectively, with the diffusion-free model predictions and experimental data of Bahga et al. [23]. Bahga et al. presented a detailed experimental study on increasing the analyte zone length by varying the channel geometry. Their channels consisted of a loading section of length L_L and large cross-sectional area, A_L, followed by a detection section with small cross-sectional area ($A_D << A_L$). The LE ion was 10 mM sodium, the TE ion was 10 mM pyridine, and the background counter-ion was 20 mM Hepes ($pK_a = 7.5$, $\mu = -23.5 \times 10^{-9}$ m^2 V^{-1} s^{-1}). In the experiments of Bahga et al., the model analyte (bistris, $pK_a = 6.4$, $\mu = 26 \times 10^{-9}$ m^2 V^{-1} s^{-1}) was injected using a semi-infinite injection scheme where analyte was mixed with TE and allowed to focus continuously over time. The initial concentration of analyte in TE, c_a^0, varied from 1 to 4 μM. Based on the experiments and a diffusion-free model, Bahga et al. [23] showed that, for a semi-infinite injection (where analyte is mixed homogenously with the TE), analyte zone length (Δ_a) in variable cross-section channel is proportional to $L_{\text{eff}} c_a^0 = (A_L L_L / A_D) c_a^0$. Here L_{eff} is the "effective length" of variable cross-section channel. It is defined as the total length of a uniform cross-section channel required to obtain the same amount of sample accumulation as the large-then-small cross-section channel system. Physically, L_{eff} is also equal to the length of channel of the smaller cross-section (with area A_D) which would have a volume equal to that swept by the ITP zone as it migrates through the large-then-small cross-sectional area channel system. Figure 6 shows a plot of the physical analyte zone length versus $L_{\text{eff}} c_a^0$ as predicted by our quasi-1D simulations, together with predictions from the diffusion-free model and experiments of Bahga et al. [23]. The quasi-1D simulations were performed for two different channel geometries with $L_{\text{eff}} = 100$ and 150 mm, each with six different initial analyte concentrations (c_a^0) ranging from 1 to 6 μM. The experiments were performed with four variable-area channel geometries, and geometric parameters are summarized in the figure. Analyte zone lengths obtained from the quasi-1D simulations show good agreement with the zone length predictions of the diffusion-free model. The diffusion-free model is in good agreement with the experiments as the conditions are such that the analyte zones are well into plateau mode (with diffusive zone boundaries significantly smaller than the plateau length) in the small cross-sectional area channel. Our simulations correctly predict experimentally observed increase in physical zone length of analyte zone versus $L_{\text{eff}} c_a^0$. As with the diffusion-free model of Bahga et al., the quasi-1D simulations presented in Fig. 6 used an experimentally estimated EOF mobility of 2×10^{-9}m^2 V^{-1} s^{-1} [23] to account for EOF in experiments.

3.4 Effect of variable channel cross-section on peak mode ITP

Lastly, we present a simulation wherein analyze zones in peak mode ITP are migrated into a converging cross-section channel to transition them into plateau mode. In ITP, analytes focus in peak mode when the analytes zones do not reach their respective plateau concentrations. Peak mode ITP tends to occur when analytes are present in trace quantities or the zone boundaries are excessively diffused due to low electric field. Direct detection of analytes focused in peak mode ITP is typically limited by their peak concentrations relative to the signal noise and background. Bottenus et al. [39]

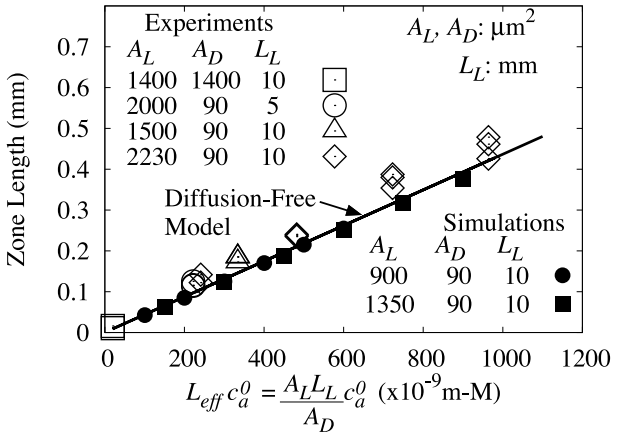

Figure 6. Comparison of experimentally observed analyte zone length in ITP in variable cross-section channels with predictions using a diffusion-free model and the current quasi-1D model. Open data points and solid line, respectively, show experimental data and results from the diffusion-free model of Bahga et al. [23]; solid data points show zone length predictions using the current simulations. Experiments and simulations involved semi-infinite injection of analyte, wherein analyte was initially mixed with TE and allowed to focus continuously over time. The channels consist of a loading section with large cross-sectional area A_L and length L_L followed by a detection section with small cross-sectional area A_D and fixed length of 7.5 mm. The plot shows analyte zone length plotted against the theoretical scaling of $L_{\text{eff}} c_a^0$ (equal to $A_L L_L c_a^0 / A_D$). The analyte is focused in plateau mode after the convergence in the channel, so the predictions using quasi-1D model are in fairly good agreement with the diffusion-free model. Further, analyte zone lengths computed using the quasi-1D model agree very well with experimentally observed linear variation of analyte zone length with $L_{\text{eff}} c_a^0$. Both experiments and simulations used 350 V applied (constant) voltage. LE ion is 10 mM sodium, TE ion is 10 mM pyridine, background counterion is 20 mM Hepes, and analyte is bistris. To account for EOF in the simulations, we used experimentally an estimated EOF mobility of 2×10^{-9}m^2 V^{-1} s^{-1} [23].

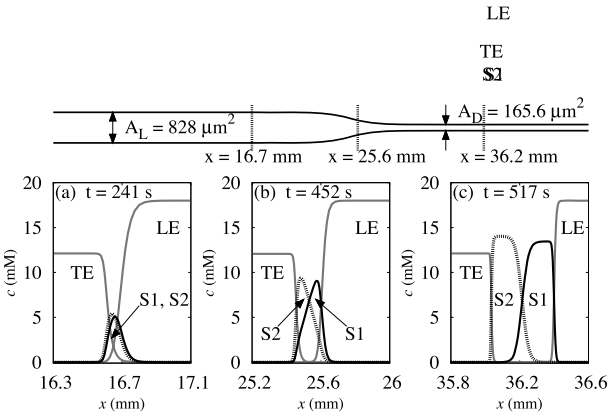

Figure 7. Simulation showing effect of variable channel cross section on peak-mode ITP. Plots (A to C) show focusing of two analytes, pyridine (S1) and aniline (S2), at three locations along a converging channel with fivefold reduction in cross-sectional area. (A) Due to their low initial concentrations, analytes S1 and S2 focus in peak mode in the large cross-section region. Peak mode focusing of analytes is characterized by largely overlapping analyte peaks with thickness comparable to the LE/TE zone boundary. (B) As the analyte zones transition from large to small cross-section region the analyte peak concentrations increase. This is in part due to relatively larger amount of sample focused per unit length of the channel, and to sharper zone boundaries associated with the higher local electric field. (C) In this particular case, when analyte zones fully migrate into the small cross-section region their zone concentrations nearly reach the plateau values determined by the Jovin and Alberty regulating functions [37, 38]. Electrolyte chemistry and channel geometry used in this simulation are the same as that in Fig. 5. Compared to the simulations shown in Fig. 5, here we used 20-fold lower amount of analytes and ten-fold lower applied current (0.1 μA) to ensure peak mode focusing of analytes in the larger cross-section channel.

experimentally demonstrated that the concentration of analytes peaks (and therefore detection sensitivity) in peak mode ITP can be increased using converging cross-sectional area channels. As analyte zones migrate from large to small cross-section region, both the local electric field and the amount of analytes focused per unit length of channel increase. Each of these effects promotes transition of peak mode focusing into plateau mode.

To illustrate the effect of variable cross-sectional area on peak mode ITP, we performed simulation of ITP focusing of two analytes (again, aniline, and pyridine for ease of comparison) in a channel with fivefold reduction in cross-sectional area. The channel geometry, analytes, and electrolyte chemistry were the same as those used for the (initially) plateau-mode ITP simulation shown in Fig. 5 and discussed above. However, to ensure peak mode focusing of analytes, we here used 20-fold less initial amount of analytes and 10-fold lower current density compared to the plateau mode ITP simulation in Fig. 5. Simulation results presented in Fig. 7 show analyte zones at three locations along the converging cross-section channel. The lower initial analyte concentrations and lower current density result in analytes focusing in peak mode in the larger cross-section region. Peak mode results in overlapping peaks focused between the TE and LE zones. As the analyte zones transition to the smaller cross-section region, their peak concentrations increase (see Fig. 7B). In this particular case, when analyte zones fully migrate into the small cross-section region (Fig. 7C) the analyte zone concentrations reach their maximum possible values determined by the Jovin and Alberty regulating functions [37, 38]. The constriction in channel cross section therefore transforms peak mode ITP to plateau mode ITP.

We note that simulations of peak mode ITP can complement experimental observations as overlapping analyte peaks are hard to identify in experiments. Also, simulations of ITP in variable cross-sectional area channels can be used to optimize the channel geometry. For example, in such systems, for constant applied current, variation of the large-to-small-channel-area ratio results in a trade off between assay time and sensitivity of plateau mode detection (see Bahga et al. [23]). Fast, high accuracy simulations of such systems can significantly reduce design and optimization time and make prototyping efforts more efficient.

4 Concluding remarks

We have developed a generalized approach for modeling and simulation of quasi-1D nonlinear electrokinetic processes in channels with axially varying cross section. Starting with 3D advection-diffusion equations, we derived quasi-1D equations for multispecies transport in terms of area-averaged quantities (species concentrations and axial electric field). Our formulation is based on typical assumptions of lubrication theory [24], including long, thin channels with slowly varying channel cross-sectional area. Our approach includes arbitrary variation in channel cross section, chemical equilibrium calculations for multivalent weak electrolytes, ionic strength effects on species mobility [11] and acid–base equilibria, and Taylor–Aris dispersion [8, 9] due to nonuniform bulk flow (due to either externally or internally generated pressure-driven flow components).

To solve the quasi-1D governing equations, we have developed a dissipative finite volume scheme which selectively adds numerical dissipation at locations with sharp gradients and oscillations. This ensures unconditional stability of the scheme, regardless of the grid size. We have also provided a novel adaptive grid refinement algorithm which improves the accuracy of our scheme by migrating grid points from regions with low numerical dissipation to regions with higher numerical dissipation. We have benchmarked our numerical method with existing numerical schemes by simulating challenging electrokinetics problems (in uniform cross-section channels) involving sharp concentration gradients. These include simulations of ITP and electromigration dispersion in CZE. Numerical experiments presented here show that the current approach yields robust and high-resolution solutions using an order of magnitude less grid points compared to existing dissipative schemes [16, 18, 35]. Also, our simulation results show reasonable agreement with nonoscillatory solutions computed using nondissipative schemes, such as the (experimentally validated) sixth-order compact scheme of Bercovici et al. [7, 14]. Unlike nondissipative schemes, the current numerical scheme is very robust as it is unconditionally stable. This feature makes our scheme advantageous for routine analysis and optimization of electrokinetic processes by researchers with little or no experience in computational methods. By comparison, nondissipative schemes may be better suited for more detailed, fundamental electrokinetics studies where accuracy is preferred over computational efficiency.

We have also demonstrated first-of-their-kind quasi-1D simulations of ITP in nonuniform cross-sectional area channels, and validated these with published experimental data. In particular, we leveraged quasi-1D simulations to predict the efficacy of converging cross-section channels in increasing detection sensitivity of both peak- and plateau-mode ITP. Until the current model, such studies have been limited to computationally expensive multidimensional simulations. The quasi-1D approach presented here is computationally efficient and hence provides new possibilities for optimization of electrokinetic systems based on shape, chemistry, or electrical control schemes to achieve high-detection sensitivity and rapid analysis. For example, simulations of ITP in converging cross-section channels can be used to determine the required amount of contraction in cross-sectional area so as to ensure complete transition from peak to plateau mode ITP. Such simulations can complement empirical designs of channel geometry and minimize trials involved in fabricating channels and performing experiments.

S. S. B. is supported by a Mayfield Stanford Graduate Fellowship and a Kodak Fellowship. We gratefully acknowledge funding from the Defense Advanced Research Projects Agency (DARPA) under grant number N660001-09-C-2082.

The authors have declared no conflict of interest.

5 References

[1] Auroux, P., Iossifidis, D., Reyes, D. R., Manz, A., *Anal. Chem.* 2002, *74*, 2637–2652.

[2] Chen, L. J. E., Fielden, P. R., Goddard, N. J., Manz, A., Day, P. J. R., *Lab Chip* 2006, *6*, 474–487.

[3] Bier, M., Palusinski, O. A., Mosher, R. A., Saville, D. A., *Science* 1983, *219*, 1281–1287.

[4] Saville, D. A., Palusinski, O. A., *AIChE J.* 1986, *32*, 207–214.

[5] Mosher, R. A., Dewey, D., Thormann, W., Saville, D. A., Bier, M., *Anal. Chem.* 1989, *61*, 362–366.

[6] Thormann, W., Zhang, C. X., Caslavska, J., Gebauer, P., Mosher, R. A., *Anal. Chem.* 1998, *70*, 549–562.

[7] Bercovici, M., Lele, S. K., Santiago, J. G., *J. Chromatogr. A* 2009, *1216*, 1008–1018.

[8] Taylor, G., *Proc. R. Soc. Lond. Ser A-Math. Phys. Sci.* 1953, *219*, 186–203.

[9] Aris, R., *Proc. R. Soc. Lond. Ser A-Math. Phys. Sci.* 1956, *235*, 67–77.

[10] Hruska, V., Jaros, M., Gas, B., *Electrophoresis* 2006, *27*, 984–991.

[11] Bahga, S. S., Bercovici, M., Santiago, J. G., *Electrophoresis* 2010, *31*, 910–919.

[12] Thormann, W., Caslavska, J., Breadmore, M. C., Mosher, R. A., *Electrophoresis* 2009, *30*, S16–S26.

[13] Dose, E. V., Guiochon, G. A., *Anal. Chem.* 1991, *63*, 1063–1072.

[14] Bercovici, M., Lele, S. K., Santiago, J. G., *J. Chromatogr. A* 2010, *1217*, 588–599.

[15] Martens, J. H. P. A., Reijenga, J. C., ten Thije Boonkkamp, J. H. M., Mattheij, R. M. M., Everaerts, F. M., *J. Chromatogr. A* 1997, *772*, 49–62.

[16] Sounart, T. L., Baygents, J. C., *J. Chromatogr. A* 2000, *890*, 321–336.

[17] Boris, J. P., Book, D. L., *J. Comp. Phys.* 1973, *11*, 38–69.

[18] Chou, Y., Yang, R. J., *J. Chromatogr. A* 2010, *1217*, 394–404.

[19] Choi, H., Jeon, Y., Cho, M., Lee, D. Y., Shim, J., *Microsyst. Technol.* 2010, *16*, 1931–1938.

[20] Hruska, V., Gas, B., Vigh, G., *Electrophoresis* 2009, *30*, 433–443.

[21] Chou, Y., Yang, R. J., *Electrophoresis* 2009, *30*, 819–830.

[22] Munson, M. S., Cabrera, C. R., Yager, P., *Electrophoresis* 2002, *16*, 2642–2652.

[23] Bahga, S. S., Kaigala, G. V., Bercovici, M., Santiago, J. G., *Electrophoresis* 2011, *32*, 563–572.

[24] Howison, S., *Practical Applied Mathematics*, Cambridge University Press, Cambridge, UK 2005.

[25] Hickman, H. J., *Chem. Eng. Sci.* 1970, *25*, 381–398.

[26] Lyklema, J., *Fundamentals of Interface and Colloid Science Volume II: Solid-Liquid Interfaces*, Academic Press, San Diego, CA 2001.

[27] Onsager, L., Fuoss, R. M., *J. Phys. Chem.* 1932, *36*, 2689–2778.

[28] Debye, P., Huckel, E., *Physik Z.* 1923, *24*, 305–325.

[29] Jameson, A., *Int J. Comput. Fluid. Dyn.* 1995, *4*, 171–218.

[30] LeVeque, R. L., *Finite Volume Methods for Hyperbolic Problems*, Cambridge University Press, Cambridge, UK 2002.

[31] Jameson, A., Vassberg, J. C., *Comput. Fluid Dyn. J.* 2000, *9*, 281–296.

[32] Palusinski, O. A., Graham, A., Mosher, R. A., Bier, M., Saville, D. A., *AIChE J.* 1986, *32*, 215–223.

[33] Ermakov, S. V., Bello, M. S., Righetti, P. G., *J. Chromatogr. A* 1994, *661*, 265–278.

[34] Khurana, T. K., Santiago, J. G., *Anal. Chem.* 2008, *80*, 6300–6307.

[35] Yu, J. W., Chou, Y., Yang, R. J., *Electrophoresis* 2008, *29*, 1048–1057.

[36] Dolnik, V., Deml, M., Bocek, P., *J. Chromatogr.* 1985, *320*, 89–97.

[37] Jovin, T. M., *Biochemistry* 1973, *12*, 871–879.

[38] Alberty, R. A., *J. Am. Chem. Soc.* 1950, *72*, 2361–2367.

[39] Bottenus, D., Jubery, T. K., Ouyang, Y., Dong, W., Dutta, P., Ivory, C. F., *Lab Chip* 2011, *11*, 890–898.

